

# Progress with Multigrid Schemes for Hypersonic Flow Problems

R. RADESPIEL

*DLR, Braunschweig, Germany*

AND

R. C. SWANSON

*NASA Langley Research Center, Hampton, Virginia 23681*

Received March 2, 1992; revised December 9, 1993

---

Several multigrid schemes are considered for the numerical computation of viscous hypersonic flows. For each scheme, the basic solution algorithm employs upwind spatial discretization with explicit multistage time stepping. Two-level versions of the various multigrid algorithms are applied to the two-dimensional advection equation, and Fourier analysis is used to determine their damping properties. The capabilities of the multigrid methods are assessed by solving three different hypersonic flow problems. Some new multigrid schemes based on semicoarsening strategies are shown to be quite effective in relieving the stiffness caused by the high-aspect-ratio cells required to resolve high Reynolds number flows. *These schemes exhibit good convergence rates for Reynolds numbers up to  $200 \times 10^6$  and Mach numbers up to 25.* © 1995 Academic Press, Inc.

---

## 1. INTRODUCTION

Over the past few years the need for efficient numerical methods to solve the equations governing hypersonic viscous flows has become very obvious. Mostly, flow solvers used in current aerospace programs, such as X-30 or SAENGER, exhibit slow convergence towards the desired steady-state solutions, which leads to high computer costs, long turn-around times, and a slowdown in the efforts to design these vehicles. The reason for this is the appearance of flow phenomena with very different scales and with highly nonlinear behavior. We mention here the laminar and turbulent boundary layers at very high Reynolds numbers and their interactions with shocks and slip lines and, furthermore, shock/shock interactions which generate complex flow fields. Many numerical techniques which were developed to assist convergence of subsonic or transonic flow calculations are found to be inappropriate for hypersonic flow applications. For example, the time step of many explicit and implicit schemes, which allows the transient behavior of strongly nonlinear hypersonic flow phenomena to be captured, is highly limited. Consequently, thousands of time steps are needed to converge the thin boundary layers.

A particular method which was successfully developed to accelerate convergence for a broad range of flow problems at both subsonic and transonic speeds is the multigrid approach. This method, which uses a sequence of successively coarser meshes in order to propagate disturbances throughout the flow field, combines nicely with explicit multistage time-stepping schemes [1]. Good convergence rates were obtained for inviscid flow and, later on, for viscous flows also [2–4]. Initial attempts to apply this promising method to hypersonic flows failed for several reasons. Primarily, the shock capturing capabilities of the central-difference scheme used in [1–4] were found insufficient to resolve strong shocks. Subsequently, the shock detection mechanism built into the central-difference scheme was improved in [5, 6]. In order to have strong shocks and slip lines resolved with fewer computational points, the central-difference scheme was replaced with an upwind-type scheme in [7–9]. Since the high-frequency damping properties of upwind schemes are generally less controllable compared with central-difference schemes, a variant of the standard multigrid approach was also used in [8, 9]. With this variant, additional coarse meshes are generated by semicoarsening in the different coordinate directions. This strategy was felt necessary to alleviate convergence problems associated with the high-aspect-ratio cells of the computational mesh. An additional problem encountered is that very high temperatures can occur in the stagnation region and near the surface at high Mach numbers; hence, the time step of explicit schemes may be severely restricted by the viscous stability limit. It was found [6, 8, 9] that the viscous time-step limit can be removed by implicit residual averaging.

It is worthwhile to note additional published work on multigrid schemes for hypersonic flows. Decker and Turkel [10] analyzed the effect of boundary conditions and Runge–Kutta coefficients on multigrid convergence for hypersonic inviscid flows. Leclercq and Stoufflet [11] analyzed two-level multigrid cycles with multistage schemes and upwind differencing in one dimension, and they presented two-dimensional computations

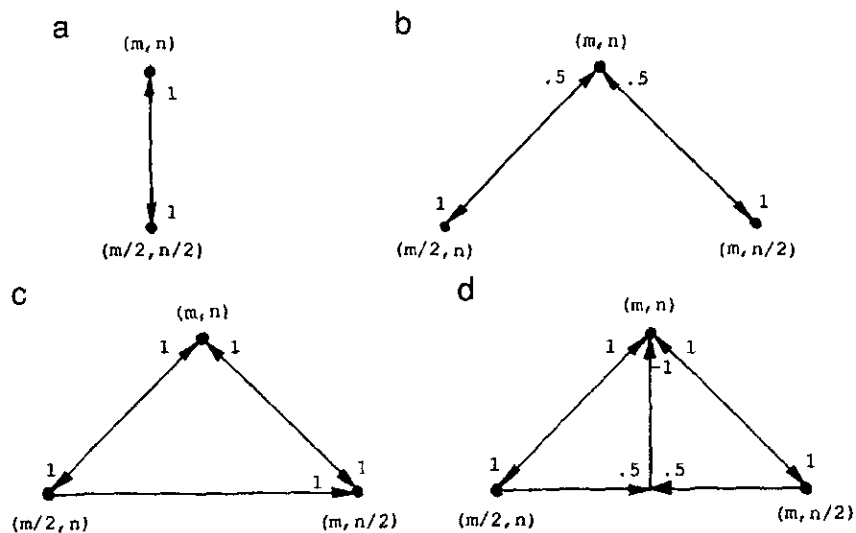


FIG. 1. Two-level multigrid schemes investigated in the present work: (a) full coarsening; (b) semicoarsening with simple averaging; (c) sequential semicoarsening; (d) semicoarsening with selective averaging.

of hypersonic flows on unstructured meshes. As a means to remove stiffness associated with high-aspect-ratio cells, Blazek *et al.* [12] introduced an upwind-biased form of the residual smoothing by which higher Courant numbers could be obtained. Thomas [13] used multigrid in combination with third-order upwind differencing and implicit approximate factorization schemes. Koren and Hemker [14] solved the steady Euler equations with multigrid and point relaxation applied as the smoother. Using damped restriction and upwind prolongation, they reported impressive convergence rates for high-speed flows around blunt bodies.

The present paper describes recent efforts to understand and to improve the use of multigrid schemes for the computation of hypersonic flows. First, various two-level multigrid schemes with and without semicoarsening are introduced. Then we use Fourier analysis of the schemes, when applied to the two-dimensional convection equation, in order to study the behavior of their components. For each multigrid approach, the solver uses upwind discretization combined with an explicit multistage scheme. We next consider the numerical solution of the Navier-Stokes equations for hypersonic flows. In Section 5, the basic elements of the flow solver for these equations are described. Some details concerning the application of the time-stepping scheme to fine and coarse grid problems are presented in the first part of Section 6. The extension of the two-level schemes to multilevel ones is then discussed. Elements of multigrid that are of particular importance for high-speed flow computations are given. In the results section, we consider three different hypersonic flow problems to assess the capabilities of the multigrid schemes. The effect of stiffness, arising from coordinate grids with high-aspect-ratio cells and from flow alignment, on the performance of the multigrid methods is examined. The benefits of semicoarsening are clearly demonstrated. Moreover,

with the semicoarsening strategies being considered, good convergence rates are obtained for Reynolds numbers up to  $200 \times 10^6$  and Mach numbers up to 25.

## 2. MULTIGRID STRATEGIES

To set the stage for the discussion relating to multigrid in subsequent sections of this paper, we first briefly describe the multigrid method and different execution strategies that will be considered. The multigrid approach is based on the *full approximation scheme* of Brandt [15]. The grid transfer operators are those considered by Jameson [1]. Coarser meshes are obtained by eliminating alternate mesh points in each coordinate direction. Both the solution and the residuals are restricted from fine to coarse meshes. A forcing function is constructed so that the solution on a coarse mesh is driven by the residuals collected on the next finer mesh. The corrections obtained on the coarse mesh are interpolated back to the fine mesh. The multigrid schemes investigated within the present work are displayed in Fig. 1. Figure 1a shows a two-level scheme with full coarsening. Restriction of the solution from the fine mesh,  $(m, n)$ , to the coarse mesh,  $(m/2, n/2)$ , is done by injection, whereas full weighting is used for the restriction of the residuals. Prolongation of the corrections is done by bilinear interpolation. Figure 1b shows a scheme with semicoarsening in the different coordinate directions. Again, injection and full weighting are used in the restriction process. The corrections obtained on the coarse meshes are averaged before adding them to the fine mesh solution. This is indicated by the numbers at the "up" arrows. Due to this averaging, half of the individual corrections on the coarse meshes is lost. It is, therefore, anticipated that the scheme in Fig. 1a should be computationally more efficient, provided there is enough high-frequency damping obtained with the smoothing

scheme of the fine mesh. In order to overcome this deficiency of the semicoarsening scheme, two more variants are considered. For the scheme of Fig. 1c, the solutions on the coarse meshes are computed sequentially. Hence, the corrections obtained on the  $(m/2, n)$  mesh can be used to update the solution on the  $(m, n/2)$  mesh before time stepping (as indicated by the horizontal arrow). The sequential update of the second coarse-mesh solution allows the full amount of corrections to be passed up to the fine mesh. Note that this multigrid variant is not compatible with the idea of parallel computations. An interesting compromise between the schemes of Figs. 1b and 1c is presented in Fig. 1d. This scheme was suggested by John Van Rosendale, and it is based on his work in [16]. Here, only the corrections common to both of the coarse meshes,  $(m/2, n)$  and  $(m, n/2)$ , are averaged, whereas the corrections to the modes living either on  $(m/2, n)$  or on  $(m, n/2)$  are passed to the fine mesh in full. This scheme does allow parallel computations for the coarse meshes.

Before proceeding some remarks concerning the relationship between the sequential semicoarsening scheme considered here and the semicoarsening scheme introduced by Mulder [17] are appropriate. According to a standard two-level Fourier analysis, where the two coarse-grid problems are solved exactly, these schemes are essentially equivalent. There is a minor difference due to the coarse-grid update in the sequential semicoarsening. These schemes can exhibit larger differences in practice due to the application of an approximate (iterative) solver on the coarse grids, the use of more than two levels, and the solution of nonlinear equations. Nevertheless, if these two schemes are used in the same multigrid method (i.e., the same iterative solver and intergrid transfer operators), one would expect them to have a similar convergence behavior.

### 3. FOURIER ANALYSIS OF THE SCALAR ADVECTION EQUATION

A crucial factor in constructing an effective multigrid method is the selection of a smoothing or driving scheme. Local mode (Fourier) analysis is generally applied to evaluate possible smoothers on the basis of stability and high-frequency damping properties. The screening of schemes is often performed with a single-grid analysis. Since a stable single-grid scheme may not be stable for the multigrid process, the behavior of a smoother with a particular multigrid strategy is needed. In addition, the multigrid process can have a substantial impact on the performance of the multigrid method. In fact, as we will demonstrate in this paper, semicoarsening can provide significant improvement, relative to full coarsening, in the damping of the multigrid, especially when there is a strong mesh anisotropy due to high-aspect-ratio cells.

A two-grid or two-level multigrid analysis has been applied by Jameson [1], Mulder [17], and Leclercq and Stoufflet [11] using various schemes (i.e., multistage time stepping, different types of relaxation) for solving the Euler and Navier–Stokes

equations of fluid dynamics. In [1] Jameson introduces a multi-level uniform analysis and considers the linear advection equation in one space dimension. This approach represents a departure from the standard two-grid analysis given by Stüben and Trottenberg [18], which forms the basis for the analysis used in [17, 11]. With the multilevel uniform analysis, fine-grid and coarse-grid corrections are computed at all points of the fine grid. Then a nonlinear filter is applied to remove the coarse-grid corrections at fine-grid points not contained in the coarse grid. The filtering produces additional errors in the form of a carrier wave with a frequency depending on the fine-mesh spacing. This analysis does not allow for the coupling (aliasing) effects due to the restriction operator (fine to coarse grid transfer operator) in the multigrid method. However, it does offer the advantages of simplicity and application to more than two-level schemes. Thus, it allows the rapid comparison of multigrid algorithms. If a multigrid method is unstable or inefficient according to this analysis, then it is probably not a reasonable scheme.

In this section, we consider the scalar two-dimensional advection equation. The multilevel uniform analysis of [1] is extended to two space dimensions and applied to full coarsening and semicoarsening strategies.

Consider an initial value problem governed by the scalar advection equation

$$\frac{\partial}{\partial t} w(x, y, t) + \mathcal{L}w(x, y, t) = 0, \quad (x, y) \in \Omega, \quad (3.1)$$

where the linear operator is

$$\mathcal{L} = a \frac{\partial}{\partial x} + b \frac{\partial}{\partial y}, \quad a > 0, b > 0,$$

the domain  $\Omega \subset \mathfrak{R}^2$ , and  $t \in \mathfrak{R}^+$ . Assume a periodic boundary condition for the scalar function  $w(x, y, t)$ . Let  $\Omega = \{(x, y) : 0 \leq x \leq 1, 0 \leq y \leq 1\}$ . Define a fine grid  $G_f$  and coarse grids  $G_{c,l}$  ( $l = 1, 2$ ) that cover the domain  $\Omega$  such that  $G_{c,l} \subset G_f$ . We generate grids  $G_{c,l}$  by eliminating every other mesh line of  $G_f$  in one or both coordinate directions. First we describe the fine-grid discrete problem. Let the grid  $G_f$  contain  $m_f \times n_f$  cells and have uniform spacings  $\Delta x_f$  and  $\Delta y_f$ . Let the discrete function  $(w_f)_{i,j}$  reside at the  $G_f$  mesh point  $(i\Delta x_f, j\Delta y_f)$ . At each point  $(i, j)$ , we consider a corresponding cell  $(C_f)_{i,j}$  with corners at  $(i - \frac{1}{2}, j - \frac{1}{2})$ ,  $(i + \frac{1}{2}, j - \frac{1}{2})$ ,  $(i + \frac{1}{2}, j + \frac{1}{2})$ , and  $(i - \frac{1}{2}, j + \frac{1}{2})$ . Suppose we approximate the spatial derivatives of (3.1) with first-order upwind differencing. Then, we obtain

$$\begin{aligned} \Delta t_f \frac{d}{dt} (w_f)_{i,j} = & -N_{\xi} [(w_f)_{i,j}^n - (w_f)_{i-1,j}^n] \\ & - N_{\eta} [(w_f)_{i,j}^n - (w_f)_{i,j-1}^n], \end{aligned} \quad (3.2)$$

where the Courant numbers are

$$N_\xi = \lambda_\xi \sigma_f, \quad N_\eta = \lambda_\eta \sigma_f$$

and

$$\lambda_\xi = a \Delta y_f, \quad \lambda_\eta = b \Delta x_f, \quad \sigma_f = \Delta t_f / \Delta \Omega_f.$$

The superscript  $n$  denotes the time level  $n \Delta t$ . If we estimate the time step  $\Delta t_f$  by

$$\Delta t_f = \frac{N \Delta \Omega_f}{a \Delta y_f + b \Delta x_f}, \quad (3.3)$$

it follows that

$$N_\xi = \frac{aN}{a + b\Lambda_f}, \quad N_\eta = \frac{bN\Lambda_f}{a + b\Lambda_f}, \quad (3.4)$$

where  $N$  is the Courant–Friedrichs–Lewy (CFL) number for an explicit time-stepping scheme, and  $\Lambda_f$  is the cell aspect ratio  $\Delta x_f / \Delta y_f$ . Taking a Fourier transform of (3.2), we obtain

$$\Delta t_f \frac{d\hat{w}_f}{dt} = -[N_\xi f(\theta_\xi) + N_\eta f(\theta_\eta)] (\hat{w}_f)^n, \quad (3.5)$$

where

$$f(\theta) = (1 - \cos \theta) + i \sin \theta,$$

and  $i = \sqrt{-1}$ . The transformed discrete function is

$$(\hat{w}_f)_{i_1, k_2}^n = \Delta x_f \Delta y_f \sum_{i_1=0}^{m_f-1} \sum_{j_1=0}^{\eta_f-1} (w_f)_{i_1, j_1}^n \exp[-i(i_1 \theta_\xi + j_1 \theta_\eta)], \quad (3.6)$$

where the phase angles  $\theta_\xi$  and  $\theta_\eta$  are given by

$$\theta_\xi = 2\pi \frac{k_1}{m_f}, \quad \theta_\eta = 2\pi \frac{k_2}{n_f},$$

with wave numbers

$$k_1 = -(\frac{1}{2}m_f - 1), \dots, \frac{1}{2}m_f, \quad k_2 = -(\frac{1}{2}n_f - 1), \dots, \frac{1}{2}n_f.$$

Equation (3.5) can be rewritten as

$$\delta \hat{w}_f = (\hat{w}_f)^{n+1} - (\hat{w}_f)^n = -Z(\theta_\xi, \theta_\eta) (\hat{w}_f)^n, \quad (3.7)$$

with  $Z$  being the Fourier symbol for the difference operator. Consider the explicit  $p$ -stage scheme

$$(w_f)^{(0)} = (w_f)^n$$

$$(\hat{w}_f)^{(l)} = (w_f)^0 - \alpha_l \sigma_f (R_f)^{(l-1)}, \quad l = 1, 2, \dots, p, \quad (3.8)$$

$$(w_f)^{(n+1)} = (w_f)^{(p)},$$

where  $R_f$  is a residual function defined as

$$R_f = \Delta \Omega_f \mathcal{L}_f w_f. \quad (3.9)$$

Using this scheme and (3.7), one can always represent the change in  $\hat{w}_f$  by

$$\delta \hat{w}_f = -\hat{F}(\theta_\xi, \theta_\eta) Z(\theta_\xi, \theta_\eta) (\hat{w}_f)^n, \quad (3.10)$$

and the symbol of the time-stepping operator  $F$  is given by

$$\begin{aligned} \hat{F}(\theta_\xi, \theta_\eta) &= \alpha_p - \alpha_p \alpha_{p-1} Z + \alpha_p \alpha_{p-1} \alpha_{p-2} Z^2 - \dots \\ &\quad - (-1)^p (\alpha_p \alpha_{p-1} \alpha_{p-2} \dots \alpha_1) Z^{p-1}. \end{aligned} \quad (3.11)$$

In (3.11) we have assumed that both the convective and numerical dissipative parts of the symbol  $Z$  are evaluated on each stage of the time-stepping scheme. Since one can write the numerical flux function as the sum of the convective and numerical dissipative contributions, one can consider a more general class of  $(p, q)$  schemes. The  $p$  refers to the number of stages, and  $q$  designates the number of evaluations of the dissipative contribution. Suppose we have a  $(p, 2)$  scheme. Let

$$Z_R = \text{Re}(Z), \quad Z_I = i \cdot \text{Im}(Z).$$

Then, if  $p \geq 3$ , the  $\hat{F}$  of (3.11) is replaced by

$$\begin{aligned} \hat{F} &= \alpha_p - \alpha_p (\alpha_1 Z_R + \alpha_{p-1} Z_I) Z_I^0 + \alpha_p \alpha_{p-1} (\alpha_1 Z_R + \alpha_{p-2} Z_I) Z_I^1 \\ &\quad - \dots - (-1)^{p-1} (\alpha_p \alpha_{p-1} \dots \alpha_3) (\alpha_1 Z_R + \alpha_2 Z_I) Z_I^{p-3} \\ &\quad + (-1)^{p-1} (\alpha_p \alpha_{p-1} \dots \alpha_1) Z Z_I^{p-2}. \end{aligned} \quad (3.12)$$

In this paper, we consider a  $(5, 3)$  scheme where the evaluations of the numerical dissipation are weighted. With such weighting, one can extend the parabolic stability limit of the scheme and/or improve the high-frequency damping behavior of the scheme. The extension of the parabolic stability limit can be important for upwind and total variation diminishing (TVD) schemes, since it provides a larger margin for the introduction of numerical dissipation. The increase in the stability interval can also be beneficial for low Reynolds number viscous flows. Another advantage of the weighted evaluation of the numerical dissipation is that the operation count of the multistage scheme can be reduced. For the  $(5, 3)$  scheme, the symbol of the residual function corresponding to the  $(k + 1)$ th stage is written as

$$\hat{R}^{(k+1)} = \sigma^{-1} \left[ Z_l \hat{w}^{(k)} + Z_R \sum_{l=0}^k \gamma_{kl} \hat{w}^{(l)} \right], \quad \sum_{l=0}^k \gamma_{kl} = 1. \quad (3.13)$$

The weighting factors are

$$\begin{aligned} \gamma_{00} &= 1, \\ \gamma_{10} &= 1, \quad \gamma_{11} = 0, \\ \gamma_{20} &= \Gamma_3, \quad \gamma_{21} = 0, \quad \gamma_{22} = \bar{\gamma}_3, \\ \gamma_{30} &= \Gamma_3, \quad \gamma_{31} = 0, \quad \gamma_{32} = \bar{\gamma}_3, \quad \gamma_{33} = 0, \\ \gamma_{40} &= \Gamma_3 \Gamma_5, \quad \gamma_{41} = 0, \quad \gamma_{42} = \bar{\gamma}_3 \Gamma_5, \quad \gamma_{43} = 0, \quad \gamma_{44} = \bar{\gamma}_5, \end{aligned} \quad (3.14)$$

where  $\Gamma_3 = (1 - \bar{\gamma}_3)$ ,  $\Gamma_5 = (1 - \bar{\gamma}_5)$ ,  $\bar{\gamma}_3 = 0.56$ , and  $\bar{\gamma}_5 = 0.44$ . The symbol of the time-stepping operator is given by

$$\begin{aligned} \hat{F} &= \alpha_5 [1 - \alpha_4 Z_l (1 - \alpha_3 Z_l) \\ &\quad - \alpha_4 Z_3 Z_l (\alpha_3 Z_2 Z_l - \bar{\gamma}_3 Z_R) - \Gamma_5 \bar{\gamma}_3 Z_3 Z_R], \end{aligned} \quad (3.15)$$

where

$$\begin{aligned} Z_1 &= Z_l + \bar{\gamma}_3 Z_R, \\ Z_2 &= Z_l + \bar{\gamma}_3 Z_R, \\ Z_3 &= \alpha_2 (1 - \alpha_1 Z_l). \end{aligned}$$

In applying multigrid to hyperbolic systems (i.e., Euler equations), or to hyperbolic-parabolic systems (i.e., Navier-Stokes equations), both signal propagation speed and damping are important, as discussed in [19]. Moreover, for the long wavelength components, the advection process is most important and multigrid achieves its efficiency by allowing the use of larger time steps on coarse grids. Hence, it is important that the smoother of the multigrid method use large time steps. For the shorter wavelength components, damping is more important, and the efficiency of multigrid is based on principles similar to those for elliptic equations.

One can extend the stability range of the explicit scheme of (3.8) with implicit residual smoothing. For two dimensions, the residual smoothing can be applied in the form

$$(1 - \beta_\xi \nabla_\xi \Delta_\xi) (1 - \beta_\eta \nabla_\eta \Delta_\eta) \bar{\mathcal{R}}_f^{(p)} = \mathcal{R}_f^{(p)}, \quad (3.16)$$

where the residual  $(\mathcal{R}_f)^{(p)}$  is defined using (3.9) as

$$(\mathcal{R}_f)^{(p)} = \sigma_f (R_f)^{(p)}, \quad (3.17)$$

$\Delta$  and  $\nabla$  are the usual forward and backward difference operators, and  $l = 1, \dots, p$ , with  $p$  being the number of stages in the scheme. The variable coefficients  $\beta_\xi$  and  $\beta_\eta$  are defined as

$$\beta_\xi = \max \left\{ \frac{1}{4} \left[ \left( \frac{N}{N^*} \frac{1}{1 + \psi r_{\eta\xi}} \right)^2 - 1 \right], 0 \right\}, \quad (3.18)$$

$$\beta_\eta = \max \left\{ \frac{1}{4} \left[ \left( \frac{N}{N^*} \frac{1}{1 + \psi r_{\eta\xi}^{-1}} \right)^2 - 1 \right], 0 \right\},$$

with  $N/N^*$  the ratio of the Courant number for the smoothed scheme to that of the unsmoothed scheme, and  $r_{\eta\xi} = \lambda_\eta / \lambda_\xi$ . A reasonable value for the parameter  $\psi$  is 0.125. In practice, this implicit procedure allows the explicit stability limit to be increased by a factor of 2 to 3. For additional details concerning implicit residual smoothing, see [3, 5].

If residual smoothing is applied on each stage of the time-stepping scheme, then the symbol  $Z(\theta_\xi, \theta_\eta)$  appearing in (3.10) and (3.11) is replaced with

$$\tilde{Z}(\theta_\xi, \theta_\eta) = \hat{S}(\theta_\xi, \theta_\eta) Z(\theta_\xi, \theta_\eta), \quad \hat{S}(\theta_\xi, \theta_\eta) = \Gamma_\xi^{-1} \Gamma_\eta^{-1}, \quad (3.19)$$

where

$$\Gamma_\xi = 1 + 2\beta_\xi (1 - \cos \theta_\xi), \quad \Gamma_\eta = 1 + 2\beta_\eta (1 - \cos \theta_\eta).$$

Before considering the discrete problem on some coarse grid  $G_{c,1}$ , we define the restriction operators and their corresponding Fourier symbols. Assume that  $G_{c,1}$  contains  $(m_f/2) \times (n_f/2)$  cells (full coarsening). Let  $T_f^c$  and  $Q_f^c$  denote the operators that transfer the fine-grid solution and residual to the coarse grid. Since any coarse-grid point belongs also to the fine grid, we have simple injection for the solution transfer operator. Thus,

$$T_f^{c,1} w_f = w_f, \quad \hat{T}_f^{c,1} = 1. \quad (3.20)$$

To ensure the conservation property for the residual transfer, we define

$$Q_f^{c,1} (R_f)_{i,j} = 4\mu_x^2 \mu_y^2 (R_f)_{i,j}, \quad (3.21)$$

where  $\mu_x$  and  $\mu_y$  are the standard averaging operators for the  $x$  and  $y$  directions. The symbol of this operator is given by

$$\hat{Q}_f^{c,1} = (1 + \cos \theta_\xi) (1 + \cos \theta_\eta). \quad (3.22)$$

If we now apply the  $p$ -stage scheme, we obtain at the corresponding point of the  $G_{c,1}$  problem

$$\begin{aligned} (w_{c,1})^{(0)} &= (w_f)^+ = (w_f)^{n+1} \\ (w_{c,1})^{(l)} &= (w_{c,1})^{(0)} - \alpha_l \sigma_{c,1} [(R_{c,1})^{(l-1)} + P_{c,1}], \quad l = 1, 2, \dots, p, \\ (w_{c,1})^{(n+1)} &= (w_{c,1})^{(p)}, \end{aligned} \quad (3.23)$$

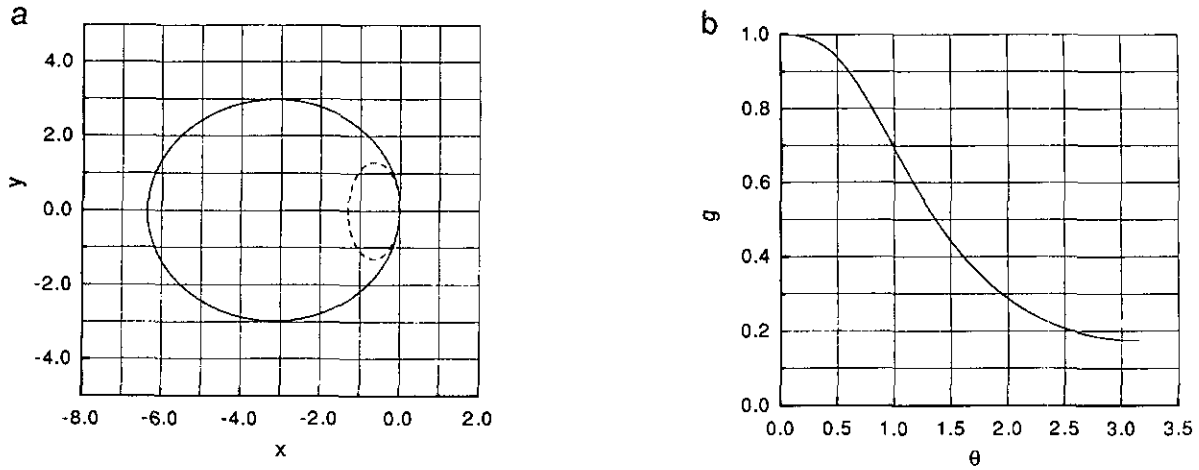


FIG. 2. Stability plots for 3-stage Runge-Kutta scheme with first-order upwind approximation (coefficients: 0.105, 0.325, 1.0): (a) stability curves with implicit residual smoothing (CFL = 5.0,  $\beta = 0.75$ ); (b) amplification factor with implicit residual smoothing (CFL = 5.0,  $\beta = 0.75$ ).

where the forcing function

$$P_{c,1} = Q_f^c(R_f)^+ - (R_{c,1})^{(0)} \quad (3.24)$$

and

$$(R_f)^+ = \Delta \Omega_f \mathcal{L}_f(w_f)^+,$$

$$(R_{c,1})^{(0)} = \Delta \Omega_{c,1} \mathcal{L}_{c,1}(w_{c,1})^{(0)}.$$

Using (3.23) and (3.24), one can easily show that

$$\delta \hat{w}_{c,1} = -\hat{F}_{c,1} \hat{S}_{c,1} \sigma_{c,1} \hat{Q}_f^c (\hat{R}_f)^+ \quad (3.25)$$

or

$$\delta \hat{w}_{c,1} = -\hat{F}_{c,1} \hat{S}_{c,1} \sigma_{c,1} \hat{Q}_f^c \sigma_f^{-1} Z_f \hat{w}_f^+ \quad (3.26)$$

with

$$(\hat{w}_f)^+ = (\hat{w}_f)^n + \delta \hat{w}_f. \quad (3.27)$$

Since

$$\delta \hat{w}_f = -\hat{F} \tilde{Z} (\hat{w}_f)^n, \quad (3.28)$$

where  $\tilde{Z}$  is the symbol of the modified difference operator defined by (3.19), then

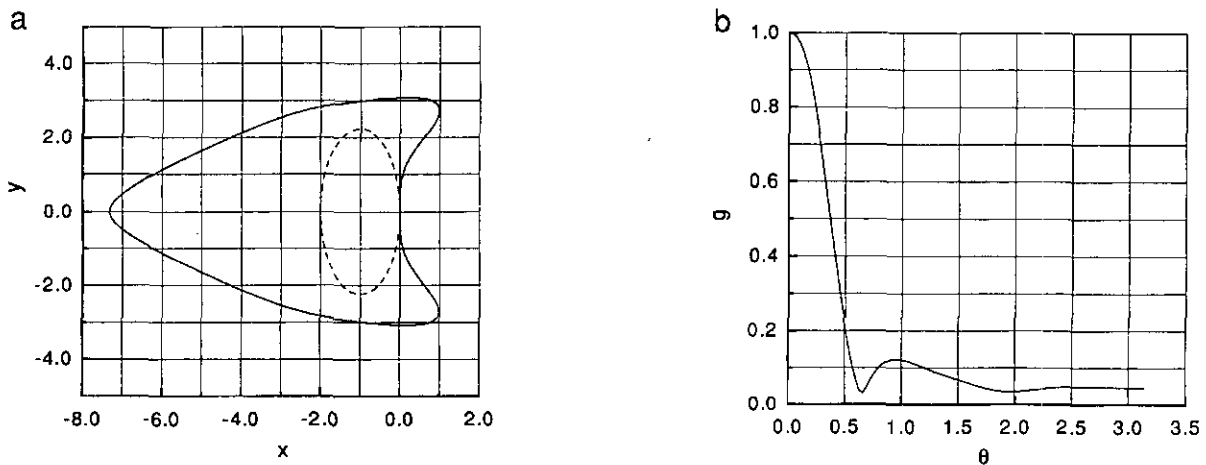


FIG. 3. Stability plots for 5-stage Runge-Kutta scheme with first-order upwind approximation and three evaluations of dissipation (coefficient: 0.2742, 0.2067, 0.5020, 0.5142, 1.0): (a) stability curves with implicit residual smoothing (CFL = 5.0,  $\beta = 1.0$ ); (b) amplification factor with implicit residual smoothing (CFL = 5.0,  $\beta = 1.0$ ).

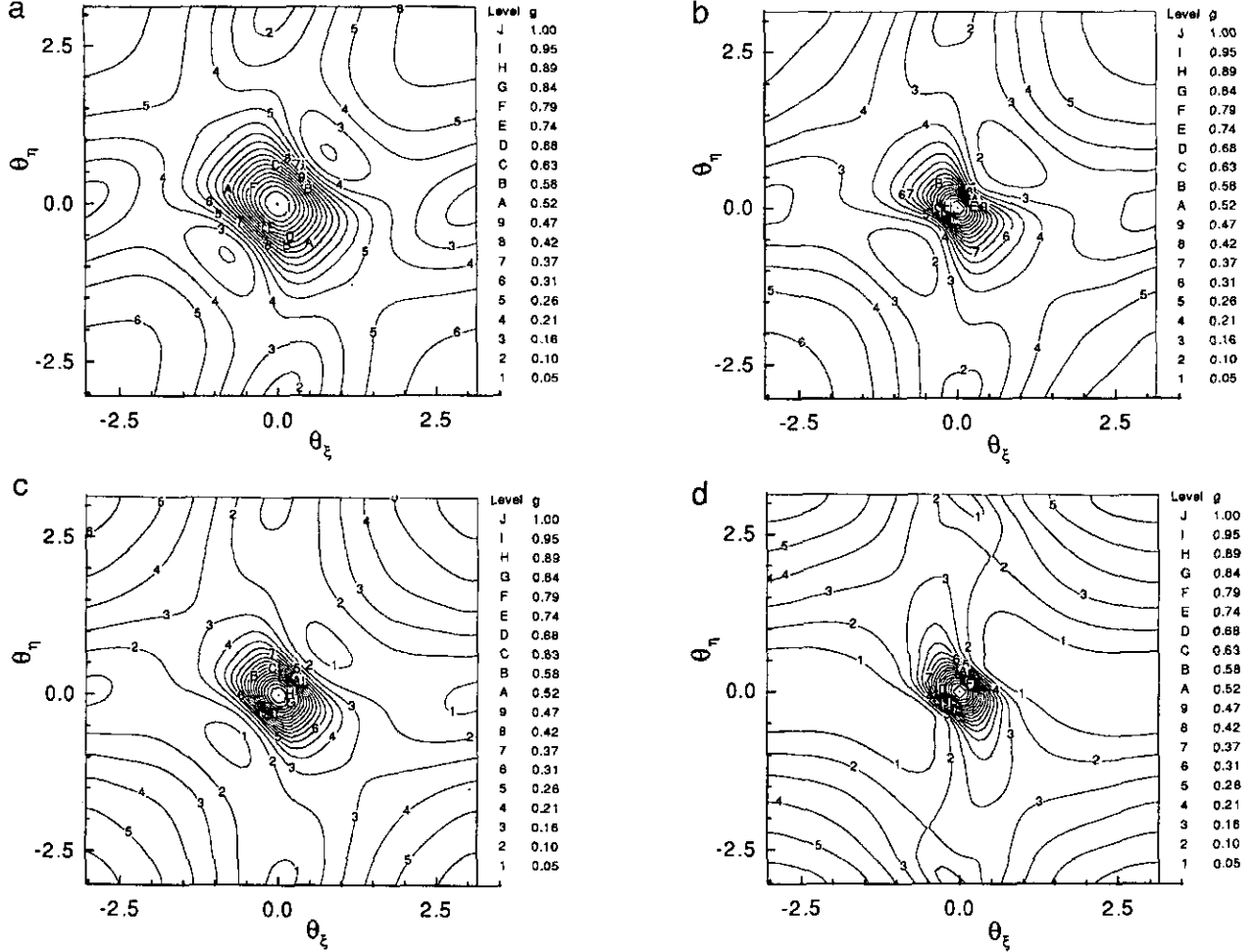


FIG. 4. Contour plots of amplification factor for 5-stage Runge–Kutta scheme with first-order upwind approximation and three evaluations of dissipation (coefficients: 0.2742, 0.2067, 0.5020, 0.5142, 1.0): (a) one level,  $\Lambda = 1$  (CFL = 5.0, CFL\* = 2.4); (b) two levels, full coarsening,  $\Lambda = 1$  (CFL = 5.0, CFL\* = 2.4); (c) two levels, semicoarsening with simple averaging, weights = 0.5,  $\Lambda = 1$  (CFL = 5.0, CFL\* = 2.4); (d) two levels, sequential semicoarsening, weights = 1.0,  $\Lambda = 1$  (CFL = 5.0, CFL\* = 2.4).

$$(\hat{w}_f)^+ = g_f(\hat{w}_f)^n, \quad (3.29)$$

where the fine-grid amplification factor is

$$g_f = 1 - \hat{F}_f \tilde{Z}_f. \quad (3.30)$$

Moreover, in this case, where we are considering full coarsening, the fine-grid approximation is

$$(\hat{w}_f)^{n+1} = (\hat{w}_f)^n + \delta \hat{w}_f + \delta \hat{w}_{c,1}$$

and, thus,

$$\begin{aligned} (\hat{w}_f)^{n+1} &= [1 - \hat{F}_{c,1} \hat{S}_{c,1} \sigma_{c,1} \hat{Q}_f^{c,1} \sigma_f^{-1} Z_f] g_f (\hat{w}_f)^n, \\ &= g_c g_f (\hat{w}_f)^n, \end{aligned} \quad (3.31)$$

with  $g_c$  denoting the coarse-grid amplification factor.

We now apply the multilevel uniform analysis to two semicoarsening multigrid strategies (see Fig. 1). Let  $G_{c,1}$  and  $G_{c,2}$  be two coarse grids containing  $(m_f/2) \times n_f$  and  $m_f \times (n_f/2)$  cells, respectively. In the case of semicoarsening with simple averaging, we express the Fourier transform of the update for the fine-grid solution as

$$(\hat{w}_f)^{n+1} = (\hat{w}_f)^n + \delta \hat{w}_f + \omega_1 \delta \hat{w}_{c,1} + \omega_2 \delta \hat{w}_{c,2}, \quad (3.32)$$

where  $\omega_1 = \omega_2 = \frac{1}{2}$ . Then the amplification factor associated with the coarse grids is given by

$$g_c = 1 - \frac{1}{2} [\hat{F}_{c,1} \hat{S}_{c,1} \sigma_{c,1} \hat{Q}_f^{c,1} \sigma_f^{-1} Z_f + \hat{F}_{c,2} \hat{S}_{c,2} \sigma_{c,2} \hat{Q}_f^{c,2} \sigma_f^{-1} Z_f]. \quad (3.33)$$

With sequential semicoarsening, we can use weightings of 1.0 for the coarse-grid corrections by improving the estimate of

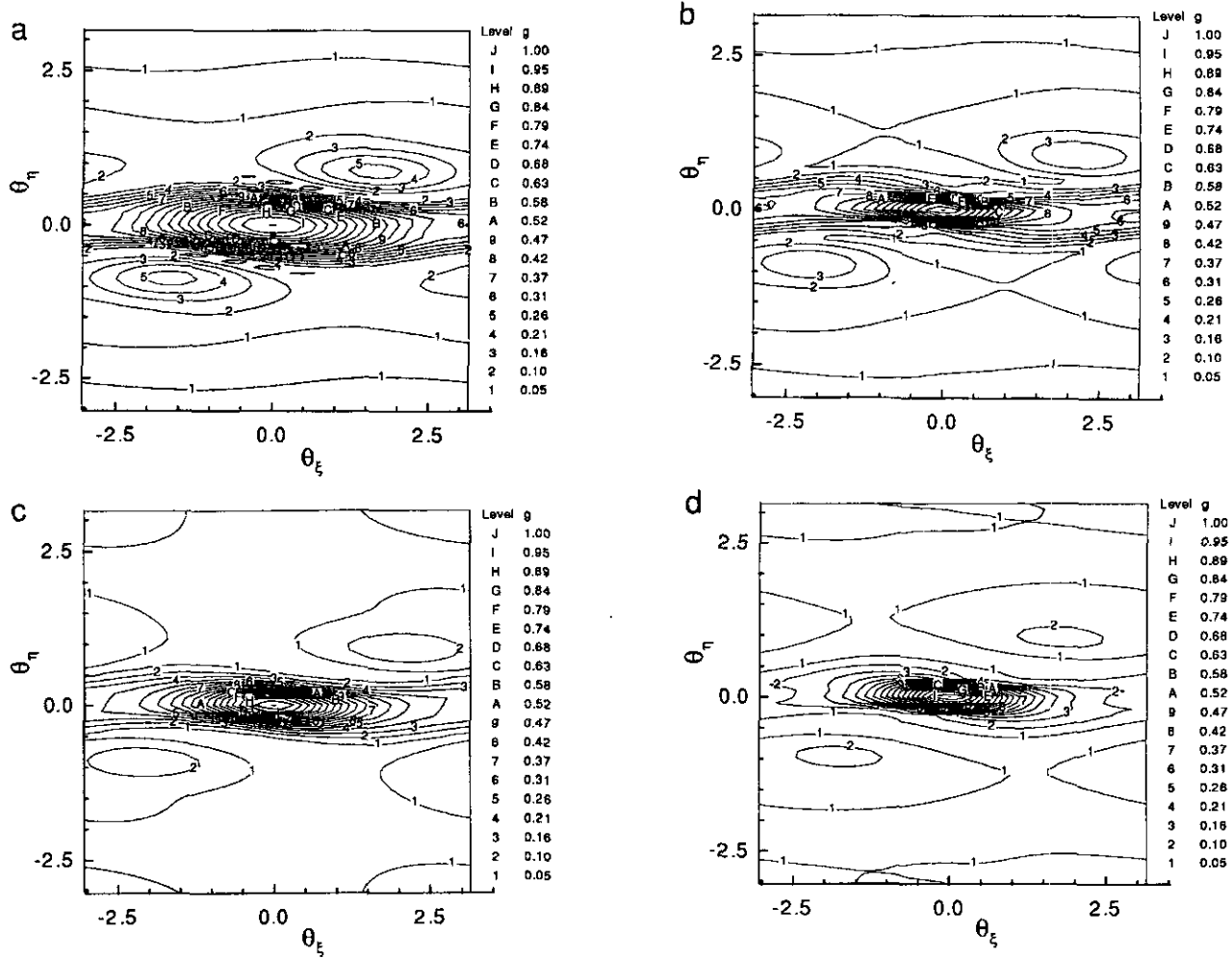


FIG. 5. Contour plots of amplification factor for 5-stage Runge-Kutta scheme with first-order upwind approximation and three evaluations of dissipation (coefficients: 0.2742, 0.2067, 0.5020, 0.5142, 1.0): (a) one level,  $\Lambda = 10$  (CFL = 5.0, CFL\* = 2.4); (b) two levels, full coarsening,  $\Lambda = 10$  (CFL = 5.0, CFL\* = 2.4); (c) two levels, semicoarsening with simple averaging, weights = 0.5,  $\Lambda = 10$  (CFL = 5.0, CFL\* = 2.4); (d) Two levels, sequential semicoarsening, weights = 1.0,  $\Lambda = 10$  (CFL = 5.0, CFL\* = 2.4).

the initial solution on either grid  $G_{c,2}$ , as indicated in Fig. 1, or  $G_{c,1}$ . The coarse-grid correction  $\delta\hat{w}_{c,1}$  is given by (3.26), and the other one  $\delta\hat{w}_{c,2}$  is given by

$$\delta\hat{w}_{c,2} = -\hat{F}_{c,2}[\hat{S}_{c,2}\sigma_{c,2}\hat{Q}_f^{c,2} - \tilde{Z}_{c,2}\hat{F}_{c,1}\hat{S}_{c,1}\sigma_{c,1}\hat{Q}_f^{c,1}]\sigma_f^{-1}Z_f g_f(\hat{w}_f)^n. \quad (3.34)$$

By substituting (3.26), (3.28), and (3.34) into (3.32), one can compute the amplification factor  $g(\theta_\xi, \theta_\eta)$ .

Before we applied the two-dimensional multigrid analysis just discussed, we examined the stability properties for a large number of multistage time-stepping schemes, including the schemes published in [20, 21]. We performed this preliminary study with the one-dimensional advection equation for a single grid. Figures 2 and 3 show two examples from this study. The dashed line represents the locus of the symbol of the difference

operator, and it must lie inside the absolute stability curve. The dissipative term for first-order upwind differencing is evaluated three times for both the three- and five-stage schemes. In the case of the (5,3) scheme, the dissipation is computed on the first, third, and fifth stages, and the weights are those given in (3.14). While the (3,3) scheme exhibits fairly good high-frequency damping, there is a substantial improvement in damping with the (5,3) scheme, at the expense of a little extra work. The coefficients for the (5,3) scheme were determined by C.-H. Tai using the analysis of [22].

In Figs. 4 and 5, we present contours of the modulus of the amplification factor for the following cases: (1) single grid; (2) full coarsening; (3) semicoarsening with simple averaging; (4) sequential semicoarsening. In the figures and in subsequent discussion we let  $g$  denote  $|g(\theta_\xi, \theta_\eta)|$ . For each case, cell aspect ratios of one and ten are shown. The improvement in damping



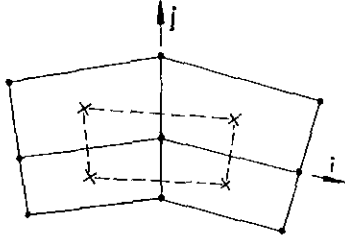


FIG. 6. Control volume for nodal-point scheme.

with the two-level schemes is evident. There is greater compression of  $g$  to the origin with the semicoarsening strategies. The aspect ratio ( $\Lambda$ ) of 10 contours indicate that the one-dimensional behavior of the driving scheme in the  $\eta$  direction is recovered for large  $\Lambda$ . They also show that modes associated with the  $\xi$  direction are damped much better with the sequential semicoarsening scheme. Moreover, let  $|\theta| = \max(|\theta_\xi|, |\theta_\eta|)$  and define the smoothing factor  $\mu$  of a scheme as the maximum  $g$  for  $0.5\pi \leq |\theta| \leq \pi$ . The  $\mu$  for the full coarsening scheme is 0.42, while the  $\mu$  for the sequential semicoarsening scheme is about 0.21.

According to the current analysis, where the nodal point of interest is assumed to be common to all meshes being considered, the semicoarsening scheme with selective averaging has the same damping behavior as the one with simple averaging. In practice, however, we observe the expected improvement in damping when using selective rather than simple averaging. This will be demonstrated later.

#### 4. GOVERNING FLOW EQUATIONS

Let  $\rho, u, v, p, T, E$ , and  $H$  denote, respectively, the nondimensional values of density, velocity components in the  $x$  and  $y$  Cartesian directions, pressure, temperature, specific total internal energy, and specific total enthalpy. In addition, let  $\mathbf{e}_x$  and  $\mathbf{e}_y$  be unit vectors of the Cartesian coordinate system  $(x, y)$  and let  $\mathbf{n}$  be a unit vector normal to the surface  $\mathcal{S}$  enclosing a volume  $\mathcal{V}$ . Then the two-dimensional, unsteady Navier–Stokes equations, neglecting body forces and heat sources, can be written in conservative form in a Cartesian coordinate system as

$$\frac{\partial}{\partial t} \iint_{\mathcal{V}} \mathbf{W} d\mathcal{V} + \int_{\mathcal{S}} (\mathcal{F}_c + \mathcal{F}_v) \cdot \mathbf{n} d\mathcal{S} = 0, \quad (4.1)$$

where the solution vector  $\mathbf{W}$  and the tensors  $\mathcal{F}_c$ ,  $\mathcal{F}_v$  are defined as

$$\mathbf{W} = \begin{bmatrix} \rho \\ \rho u \\ \rho v \\ \rho E \end{bmatrix}, \quad \mathcal{F}_c = \begin{bmatrix} \rho u \mathbf{e}_x + \rho v \mathbf{e}_y \\ (\rho u^2 + p) \mathbf{e}_x + \rho u v \mathbf{e}_y \\ \rho u v \mathbf{e}_x + (\rho v^2 + p) \mathbf{e}_y \\ \rho u H \mathbf{e}_x + \rho v H \mathbf{e}_y \end{bmatrix},$$

$$\mathcal{F}_v = \widetilde{\text{Re}}^{-1} \begin{bmatrix} 0 \\ \sigma_x \mathbf{e}_x + \tau_{xy} \mathbf{e}_y \\ \tau_{xy} \mathbf{e}_x + \sigma_y \mathbf{e}_y \\ (u\sigma_x + v\tau_{xy} - q_x) \mathbf{e}_x \\ + (u\tau_{xy} + v\sigma_y - q_y) \mathbf{e}_y \end{bmatrix},$$

with

$$\sigma_x = -\lambda \left( \frac{\partial u}{\partial x} + \frac{\partial v}{\partial y} \right) - 2\mu \frac{\partial u}{\partial x},$$

$$\sigma_y = -\lambda \left( \frac{\partial u}{\partial x} + \frac{\partial v}{\partial y} \right) - 2\mu \frac{\partial v}{\partial y},$$

$$\tau_{xy} = \tau_{yx} = -\lambda \left( \frac{\partial u}{\partial y} + \frac{\partial v}{\partial x} \right),$$

$$q_x = k \left( \frac{\partial T}{\partial x} \right),$$

$$q_y = k \left( \frac{\partial T}{\partial y} \right),$$

$$H = E + \frac{p}{\rho}.$$

The scaling factor  $\widetilde{\text{Re}}^{-1} = \sqrt{\gamma} M \text{Re}^{-1}$ , with  $M$  and  $\text{Re}$  representing the Mach and Reynolds numbers, respectively. In this paper, the working fluid is air, and it is assumed to be thermally and calorically perfect. That is, the equation of state is

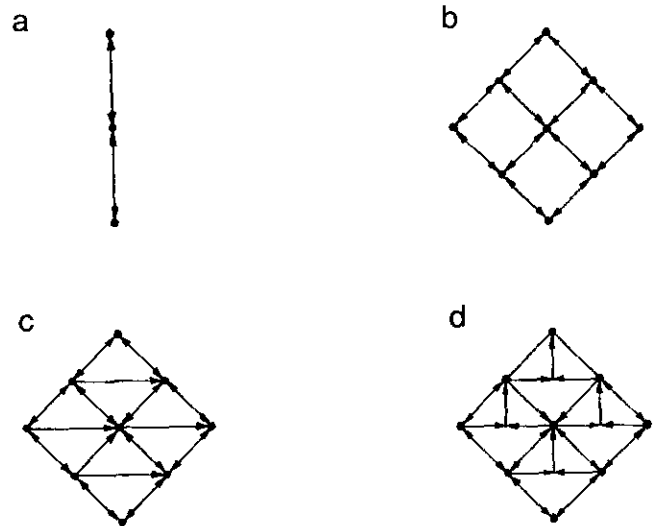


FIG. 7. Multilevel schemes: (a) full coarsening; (b) semicoarsening with simple averaging; (c) sequential semicoarsening; (d) semicoarsening with selective averaging.

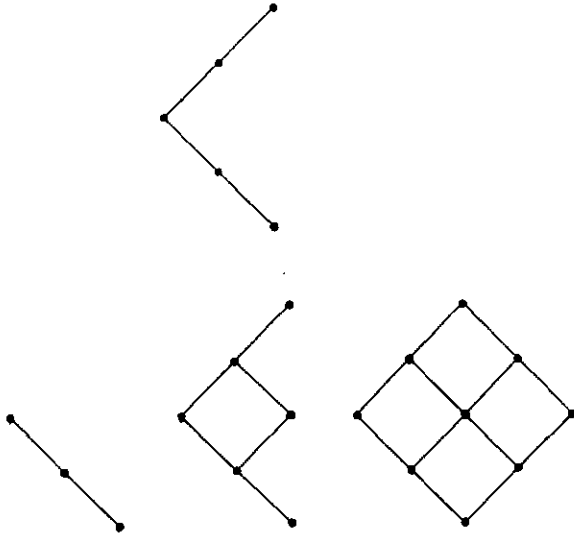


FIG. 8. Semicoarsening with selection of coarse meshes.

$$p = (\gamma - 1)\rho(E - (u^2 + v^2)/2), \quad T = p/\rho. \quad (4.2)$$

The quantities  $\mu$  and  $\lambda$  are the first and second coefficients of viscosity, respectively, and  $\lambda$  is taken to be  $-\frac{2}{3}\mu$  (Stokes hypothesis). Sutherland's law is used to determine the molecular viscosity coefficient  $\mu$ . The coefficient of thermal conductivity ( $k$ ) is evaluated using the constant Prandtl number assumption. The effect of turbulence is taken into account by using the eddy viscosity hypothesis. In the present work, the turbulence model of Baldwin and Lomax [23] is used.

## 5. SPATIAL DISCRETIZATION

The numerical approximation of (4.1) follows the method of lines, which decouples the discretization in space and time. The physical domain around the aerodynamic body is divided into quadrilateral cells by the generation of a body-fitted grid. The discrete values of the flow quantities are located at the vertices of the mesh cells. For the flux calculation, an auxiliary

grid is used, which is defined by connecting the cell centers of the original cells (see Fig. 6). The integral equation (4.1) is approximated by the spatial discretization, yielding

$$\frac{d}{dt} \mathbf{W}_{i,j} = -\frac{1}{V_{i,j}} ((\mathbf{Q}_c)_{i,j} + (\mathbf{Q}_v)_{i,j}), \quad (5.1)$$

where  $V_{i,j}$  denotes the area of the control volume surrounding the grid node  $(i, j)$ ;  $(\mathbf{Q}_c)_{i,j}$  and  $(\mathbf{Q}_v)_{i,j}$  represent approximations of the convective flux and viscous flux, respectively. The viscous fluxes are approximated by central differences using a local transformation from Cartesian coordinates to the curvilinear coordinates [4]. In the following some details of the upwind discretization of the convective terms are discussed. The inviscid flux through the interface,  $(i + \frac{1}{2}, j)$  is evaluated as

$$(\mathbf{Q}_c)_{i+1/2,j} = \frac{1}{2}[(\mathcal{F}_c)_{i,j} + (\mathcal{F}_c)_{i+1,j}] \cdot \mathbf{S}_{i+1/2,j} + \frac{1}{2}R_{i+1/2,j} \Phi_{i+1/2,j}. \quad (5.2)$$

Here,  $\mathbf{S}_{i+1/2,j}$  is the surface vector of face  $(i + \frac{1}{2}, j)$ , and  $R$  is the right eigenvector matrix of the flux Jacobian in transformed space. Equation (5.2) separates the inviscid numerical flux into the sum of an averaged term corresponding to central differencing and a dissipative term, which adapts the discretization stencil in accordance with local wave propagation. The flux function  $\Phi$  is based on the second-order accurate upwind TVD scheme of Yee and Harten [24]. Here, we do not repeat the formulation for  $\Phi$ , but simply indicate some important details in the present numerical evaluation of  $\Phi$ . Second-order accuracy is obtained with the limiter

$$g_{i,j} = \frac{\alpha_{i-1/2,j}(\alpha_{i+1/2,j}^2 + \varepsilon) + \alpha_{i+1/2,j}(\alpha_{i-1/2,j}^2 + \varepsilon)}{\alpha_{i-1/2,j}^2 + \alpha_{i+1/2,j}^2 + 2\varepsilon}, \quad (5.3)$$

where  $\alpha$  is the first difference of the characteristic variable,  $R^{-1}\Delta\mathbf{W}$ , and  $\varepsilon$  is a small constant to prevent division by zero. The flow quantities at the face  $(i + \frac{1}{2}, j)$  are evaluated by Roe's averaging procedure [25]. The limiter function of (5.3) was selected because numerical experimentation with alternative limiter functions given by Yee [26] showed less reliable conver-

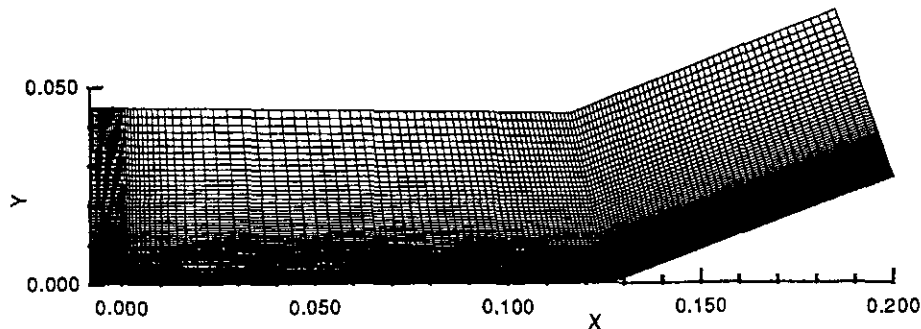


FIG. 9. Coordinate mesh for ramp-flow problem with  $128 \times 80$  cells.

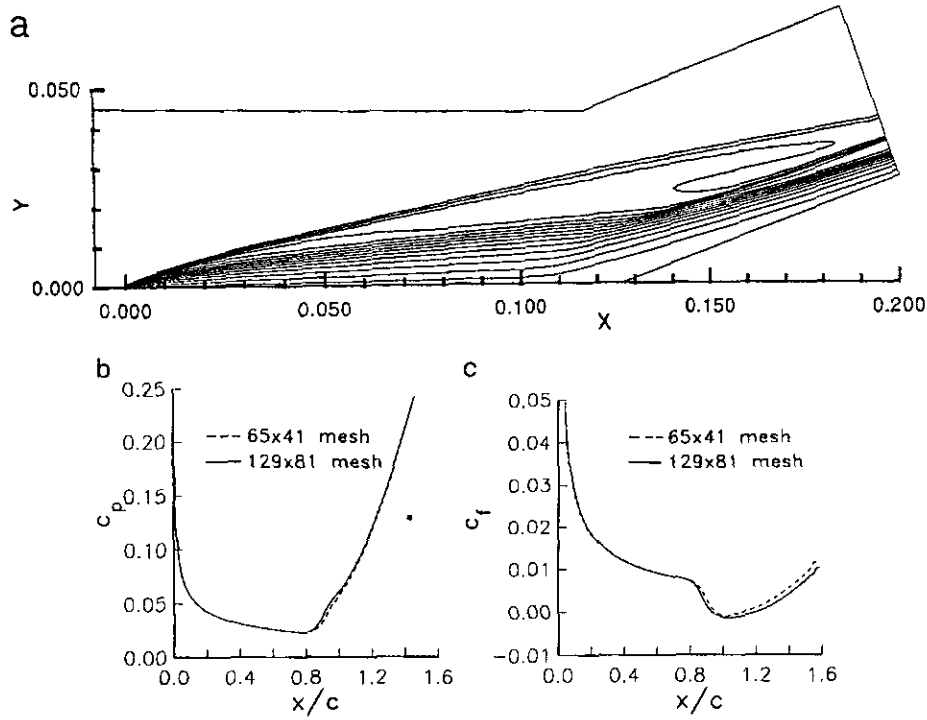


FIG. 10. Flow solution for ramp-flow problem: (a) Mach contours; (b) pressure coefficient; (c) skin friction.

gence behavior in general. Note that the scheme is identical to Roe's first-order flux difference splitting for  $g = 0$ . Since Roe's scheme may violate the entropy condition when the eigenvalues of the flux Jacobians vanish, the eigenvalues are modified using an entropy function  $\Psi$ . This entropy correction has to be carefully designed for viscous flow calculations. The shear layers along solid walls are numerically smeared if an entropy correction is applied to the eigenvalues associated with the convective waves. On the other hand, if cells with high aspect ratios are present, additional support for damping in the direction of the long side of a cell is needed in regions of low velocities, such as stagnation points. Therefore, the correction of the eigenvalues  $\Psi$  is constructed as a function of the cell aspect ratio. For the convective waves, the function

$$\Psi(\lambda_\xi^l) = \begin{cases} |\lambda_\xi^l|, & \text{if } |\lambda_\xi^l| \geq \delta, \\ \beta \frac{|\lambda_\xi^l|^2 + \delta^2}{2\delta} + (1 - \beta)|\lambda_\xi^l|, & \text{otherwise,} \end{cases} \quad (5.4)$$

and for the acoustic waves,

$$\Psi(\lambda_\xi^l) = \begin{cases} |\lambda_\xi^l|, & \text{if } |\lambda_\xi^l| \geq \delta, \\ \frac{|\lambda_\xi^l|^2 + \delta^2}{2\delta}, & \text{otherwise.} \end{cases} \quad (5.5)$$

In Eqs. (5.4) and (5.5),  $\lambda_\xi^l$  represents the  $l$ th eigenvalue of the

transformed flux Jacobian in the  $\xi$ -direction. The entropy parameter,  $\delta$ , is given according to Müller [27],

$$\delta = \tilde{\delta} \lambda_\xi (1 + (\lambda_\eta / \lambda_\xi)^\omega), \quad (5.6)$$

where  $\lambda_\xi$ ,  $\lambda_\eta$  are the spectral radii of the flux Jacobians in the  $\xi$  and  $\eta$  directions,  $0 < \omega < 1$ , and  $0.1 < \tilde{\delta} < 0.5$ . If  $\mathbf{U} = u\mathbf{e}_x + v\mathbf{e}_y$ ,  $\mathbf{S}_\xi$  and  $\mathbf{S}_\eta$  are directed areas associated with the  $\xi$  and  $\eta$  directions, and  $c$  is the speed of sound, then

$$\lambda_\xi = |\mathbf{U} \cdot \mathbf{S}_\xi| + c|\mathbf{S}_\xi|, \quad \lambda_\eta = |\mathbf{U} \cdot \mathbf{S}_\eta| + c|\mathbf{S}_\eta|. \quad (5.7)$$

The blending coefficient,  $\beta$ , accounts for the cell aspect ratio. It is given as

$$\beta = \max(1 - \lambda_\xi / \lambda_\eta, \kappa). \quad (5.8)$$

It is shown below that  $\kappa$  should be zero for accurate computations of shear layers. Furthermore, we will demonstrate that a wide range of flow problems can be solved accurately with a single set of parameters,  $\tilde{\delta} = 0.25$ ,  $\omega = 0.3$ , and  $\kappa = 0$ .

## 6. ITERATIVE SCHEME FOR HYPERSONIC FLOWS

The basic elements of the time-stepping scheme have been outlined in Section 3, and they are not repeated here. In the

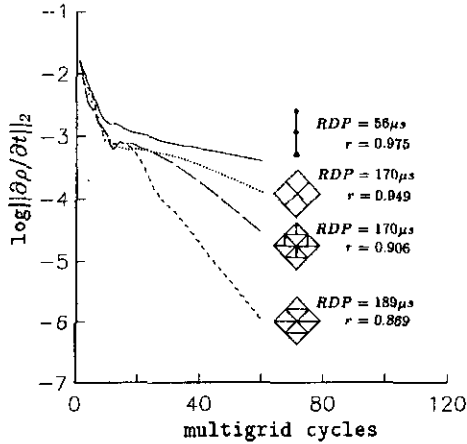


FIG. 11. Influence of multigrid strategies on convergence for ramp-flow problem.

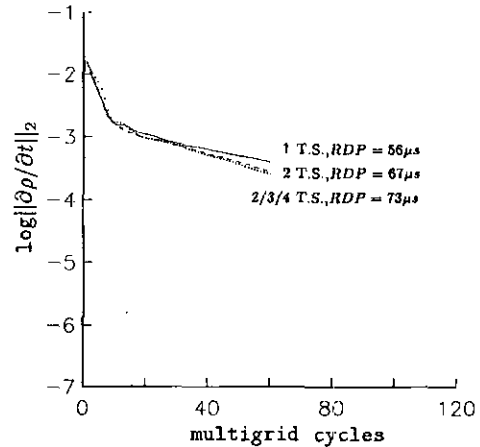


FIG. 13. Influence of multiple time stepping on coarse meshes for multigrid with full coarsening.

following sections emphasis is placed on recent improvements to enhance robustness for hypersonic flow calculations.

6.1. Multistage Scheme for the Fine and Coarse Meshes

Consistent with the results for the advection equation in Section 3, we have observed the need to pair spatial discretization and particular time-stepping schemes for the solution of the Navier–Stokes equation. The most robust choice of spatial discretizations found to this point is to use the second-order upwind scheme of Section 5 on the fine meshes and to set the limiter to zero everywhere on the coarse meshes. An alternative choice taken in [6, 8] is to use scalar second-difference dissipation terms on the coarse meshes. This turned out to be less robust because the second differences are less diffusive with respect to the acoustic modes; also, the central-difference scheme allows waves to travel upstream in supersonic flow. As indicated previously, a five-stage scheme with three evalua-

tions of dissipation and the coefficients of Tai [22] is used for time advancement. The large viscous stability limit of this scheme is shown in Fig. 3. Disturbances are most effectively expelled out of the computational domain by using local time stepping and implicit residual smoothing [5, 6]. The smoothing of the residuals allows a Courant number ratio (CFL/CFL\*) as high as 2.5 when CFL\* = 2.3, which is roughly the stability limit of the explicit scheme. The time step is determined by the spectral radii of the inviscid flux Jacobians in the different coordinate directions,  $\lambda_\xi$  and  $\lambda_\eta$ , as

$$\Delta t = CFL \frac{V}{\lambda_\xi + \lambda_\eta}. \tag{6.1}$$

In order to stabilize the schemes in regions where the viscous stability limit is more restrictive than the inviscid limit, the coefficients of the implicit residual smoothing operator are

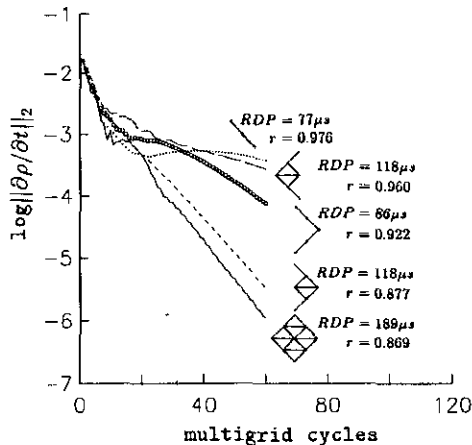


FIG. 12. Influence of selected coarse meshes on convergence for ramp-flow problem.

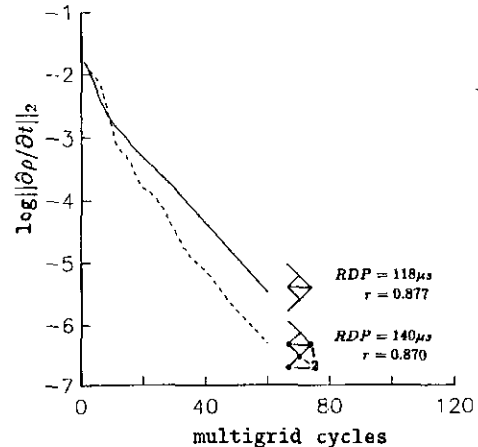


FIG. 14. Influence of multiple time stepping on coarse meshes for multigrid with sequential semicoarsening.

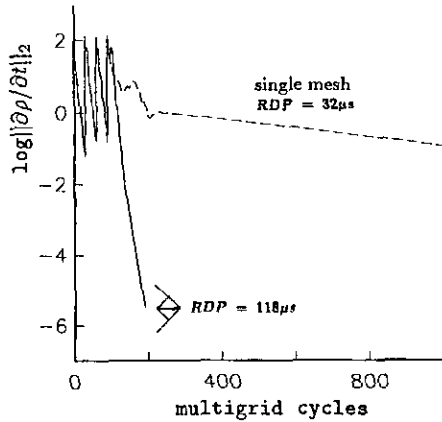


FIG. 15. Convergence of ramp flow with single-mesh time stepping and multigrid with sequential semicoarsening.

locally increased, as outlined in [6, 8]. At strong shocks, however, high Courant numbers are not appropriate. Consequently, an adaptive time step is employed. By using the nondimensional second difference of the pressure as a switch, the value of CFL is locally reduced to about two at the shock.

## 6.2. Multigrid Schemes

For the numerical solution of the Navier–Stokes equations, the two-level strategies presented in Fig. 1 are extended to multilevel schemes, as displayed in Fig. 7. The only differences between the two-level schemes and the multilevel schemes occur in the restriction process. Whenever two “down” arrows meet at a coarse mesh, averaging is used to obtain the restricted variable. The multilevel arrangement of the coarse meshes, shown in Fig. 7b, was first given by Mulder [17], who used semicoarsening in order to solve the flow alignment problem. Suitable coordinate meshes for thin boundary layers exhibit mostly cells with high aspect ratios in the surface-aligned direction. Figure 8 displays further variants of semicoarsening for these situations which are computationally cheaper than the semicoarsening schemes shown in Fig. 7.

One may notice that the central restriction and prolongation operators discussed in Section 2 allow for upstream propagation of disturbances in supersonic flow. Furthermore, the corrections given by the standard multigrid scheme near strong shocks lead to divergence of the calculation, particularly during the initial part of the transient phase. Therefore, the restriction operator is damped by using

$$R_{i,j} = \max(1 - \varepsilon_{i,j}^{(n)}, 0) \bar{R}_{i,j}, \quad (6.2)$$

where  $\bar{R}_{i,j}$  is the standard restriction operator and  $\varepsilon_{i,j}^{(n)}$  is a switch to detect strong shocks:

$$\varepsilon_{i,j}^{(n)} = k^{(n)} \max(v_i, v_{i+1}, v_{i-1}, v_j, v_{j+1}, v_{j-1}), \quad (6.3)$$

$$v_i = \left| \frac{p_{i-1,j} - 2p_{i,j} + p_{i+1,j}}{p_{i-1,j} + 2p_{i,j} + p_{i+1,j}} \right|, \quad v_j = \left| \frac{p_{i,j-1} - 2p_{i,j} + p_{i,j+1}}{p_{i,j-1} + 2p_{i,j} + p_{i,j+1}} \right|. \quad (6.4)$$

The damping coefficient,  $k^{(n)}$ , is given a value of about one in the startup phase of the multigrid process and is decreased to a value of about 0.4 at later cycle numbers in order to allow for improved asymptotic convergence rates. This is in line with the restriction damping of Koren and Hemker [14], who based their damping coefficients on a more physical analysis. Numerical results obtained for different choices of  $k^{(n)}$  are given in the next section.

A fixed V-type cycle with time stepping on the way down is used to execute the multigrid strategies described above. The robustness of the overall scheme is much improved by smoothing the resultant coarse-mesh corrections before they are passed to the finest mesh. The smoothing reduces high-frequency oscillations introduced by the linear interpolation of the coarse-mesh corrections. The factored scheme equation (3.16) with constant coefficients around 0.1 is used for this smoothing. Also, the application of full multigrid (FMG) provides a well-conditioned starting solution for the finest mesh being considered.

One could choose another type of multigrid cycle. In fact, based on our experience with solving fluid dynamics problems, FMG with V-type cycles converges slower than FMG with W-type cycles. However, usually the computational time to achieve a certain level of convergence is roughly the same. In addition, we have found that with the class of multigrid schemes being considered, a V-type cycle with two sweeps of each coarse mesh yields about the same convergence history as a W-type cycle.

## 7. NUMERICAL RESULTS

Four different flow problems are considered to assess the capabilities of the multigrid schemes. There are three hyper-

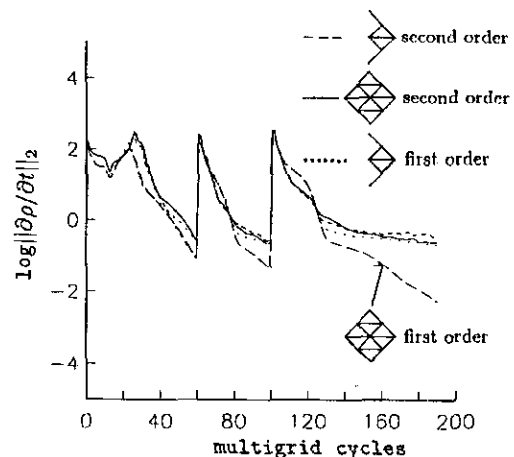


FIG. 16. Convergence histories for flow-alignment problem.

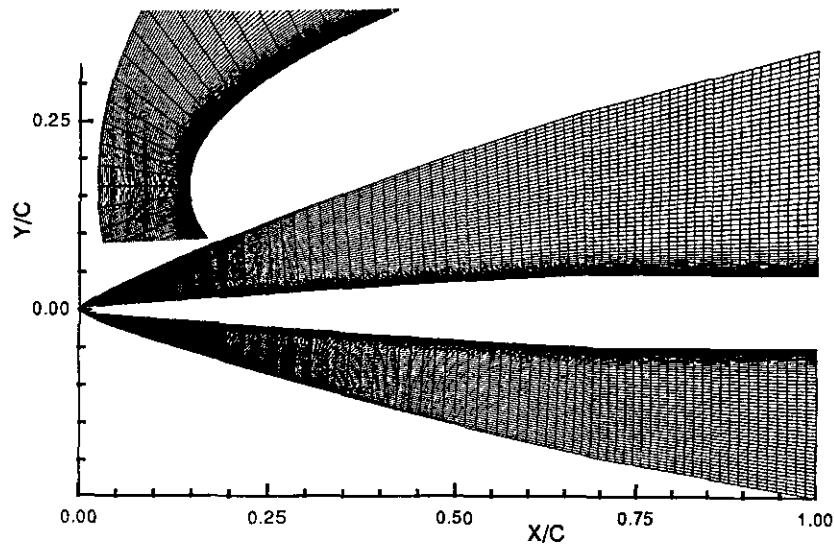


FIG. 17. Coordinate mesh for forebody with  $256 \times 96$  cells.

sonic flow cases. These are laminar Mach 10 ( $M = 10$ ) flow over a compression ramp, turbulent flow over a slender forebody at high Reynolds number, and laminar flow over an airfoil at high Mach number and high angle of attack. The fourth case, which involves transonic flow over an airfoil, is used to indicate the behavior of the multigrid method with sequential semicoarsening for lower Mach numbers. This particular case was selected because it has a large numerical data base. Table 1 gives a summary of the geometries and the flow parameters of the test cases. In this table,  $T_{inf}$  is the dimensional free-stream temperature, and  $T_w$  is the specified wall temperature. Also, the finest grid used for each flow computation is characterized by the streamwise and normal leading-edge spacings ( $\Delta s_{le}$ ,  $\Delta n_{le}$ ),

along with the normal spacing ( $\Delta n_{te}$ ) at the end or trailing edge of a geometry.

The flow over the compression ramp is identical to Case 3.2 of the *Workshop on Hypersonic Flows for Reentry Problems, Part II, Antibes, France, 1991*. This allows comparisons with the performance of other computational methods published in [28]. Figure 9 displays the coordinate mesh generated for this test case. The low Reynolds number allows for a mesh with moderate aspect ratios between 5 and 50 near the wall. The  $129 \times 81$  mesh is successively coarsened down to  $9 \times 6$ , which yields nine grid levels with semicoarsening and five levels with full coarsening. It is expected that the semicoarsening strategy should eliminate most of the stiffness associated with aspect

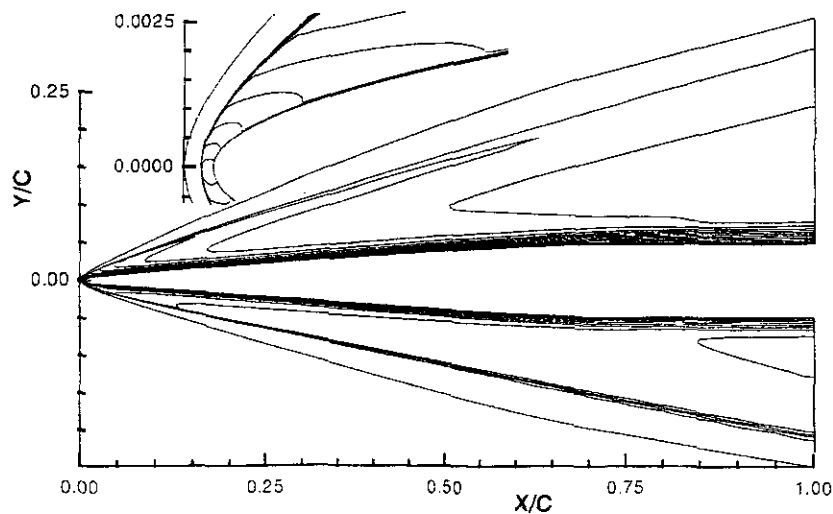
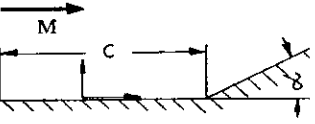
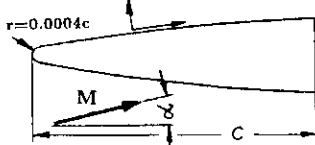
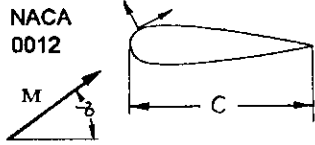
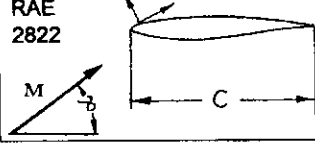


FIG. 18. Mach contours for turbulent forebody.

Table I  
Flow Parameters and Geometric Parameters for the Test Cases

Flow Case	$M$	$\alpha$	$Re_c$	$T_{inf}$	$T_w/T_{inf}$	No.Pts.	$\Delta s_{te}/c$	$\Delta n_{te}/c$	$\Delta n_{te}/c$
	10	20°	18119	52K	5.57	129x81	0.004	0.0008	0.0008
	7	5°	2.E8	100K	adiab.	257x97	4.4E-5	2.E-7	2.E-6
	25	30°	2.E5	100K	50	257x81	1.3E-3	1.E-5	1.E-4
	0.73	2.79°	6.5E6	273K	adiab.	321x65	1.6E-3	1.E-5	1.E-5

ratio. The converged flow solution is shown in Fig. 10. The computed extent of separation in the corner is somewhat smaller for the coarse mesh than for the fine mesh. Note that the result of the fine mesh agrees very well with grid-converged computations published in [13].

In the next figures, we investigate the performance of the different multigrid schemes. For this purpose, computations are started from a solution which was converged to about plotting accuracy. Figure 11 compares the different schemes of Fig. 7. The numbers indicate the final convergence rate ( $r$ ) of the schemes and the rate of data processing (RDP) on a Cray-YMP to advance one grid point by one multigrid cycle. It is seen that the sequential semicoarsening scheme (Fig. 7c) gives by far the best convergence rate. For this scheme, the effect of the modifications shown in Fig. 8 is investigated in Fig. 12. One finds that the meshes obtained by full coarsening and by semicoarsening in the direction normal to the wall are both important to achieve good convergence rates. From Figs. 11–12, we conclude that semicoarsening with a selected number of coarse meshes is most effective for this flow problem; however, full coarsening does a surprisingly good job because of its low work count. The convergence rates indicated in Figs. 11–12 were obtained with the damping coefficient  $k^{(n)}$  set at 0.3. By increasing  $k^{(n)}$  to 1.0, which is a typical value for the initial phase of the calculations, one observes slightly worse

rates. For example, the rate ( $r$ ) of 0.877 for sequential semicoarsening with coarse-mesh selection, which is given in Fig. 12, decreases to  $r = 0.893$ . On the other hand, decreasing the value of  $k^{(n)}$  yields divergence of the computation. Figures 13–14 show improvements which may be gained by using more than a single time step on the coarse meshes. The full coarsening scheme, Fig. 13, gives only marginal gains when using more than two time steps on the coarse meshes. The sequential semicoarsening scheme, Fig. 14, gives an initially improved rate, whereas the final rate is not affected by more work done on the coarse meshes. It is thought that the capabilities of the multigrid approach are put to full use for this test case. Further improvements are foreseen only if the remaining stiffness in the discrete equations, that is the differences in the characteristic speeds of acoustic and convective waves, can be overcome by some proper means. A comparison between single mesh and multigrid computations is given in Fig. 15. We find that the multigrid scheme with sequential semicoarsening converges within one-tenth of the computing time required for the single mesh scheme.

The grid generated for the ramp flow is well suited to study the grid-alignment problem which occurs for inviscid flow over the ramp. Figure 16 shows convergence histories of various schemes obtained by using a slip-wall boundary condition and omitting the viscous terms in the governing equations. Gener-

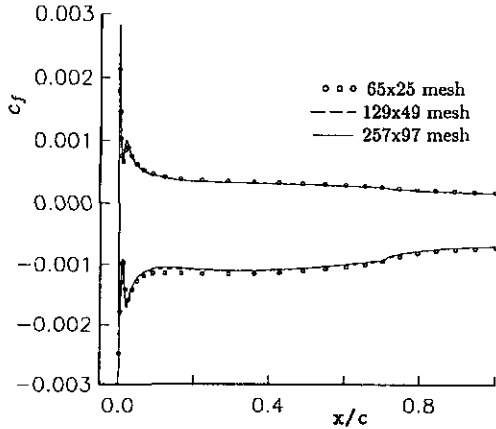


FIG. 19. Distribution of skin friction along forebody.

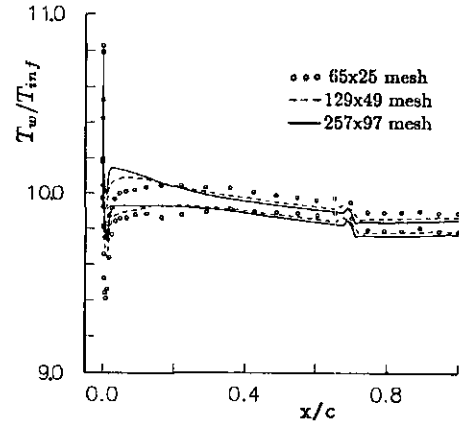


FIG. 20. Distribution of adiabatic wall temperature along forebody.

ally, convergence is worse for the inviscid flow because the convective eigenvalues of the flux Jacobian in the normal direction are zero for most of the grid points. The second-order solution does not converge, regardless of which multigrid strategy we use. With the flux limiter, Eq. (5.3), set to zero everywhere on the fine mesh, the solution converges, provided we use all the coarse meshes introduced by the semicoarsening approach. For this problem perfect flow alignment does not occur. In particular, the differential operator for the direction normal to the flow vanishes, but the corresponding discrete operator does not. This nonalignment is caused by the discretization and iteration errors. One might conclude that the stalled convergence with the second-order upwind scheme is primarily a consequence of nonalignment. However, since the rate of convergence with the first-order approximations of the spatial derivatives is somewhat slow, which is not consistent with the results of Mulder [29] with semicoarsening, it is reasonable to conclude that nonalignment is not the only source of difficulty. Another fact to consider is that the explicit iteration scheme is

somewhat less effective in damping shear waves than acoustic waves. This is because the size of the time step is dominated by the acoustic wave speed. Preconditioning techniques such as those of [30, 31], which attempt to equilibrate wave speeds, could possibly improve this situation considerably.

The flow over a slender forebody is chosen to represent a generic configuration corresponding to a high-speed civil transport aircraft or an air-breathing space transportation system with low wave drag. The high Reynolds numbers yield thin boundary layers, which can only be resolved with highly clustered coordinate meshes and large aspect ratio cells. The mesh used for the present investigations is displayed in Fig. 17. The cells near the wall have aspect ratios up to 25,000. The flow computations were done with fixed transition at 2% chord and with the assumption of an adiabatic wall. Figures 18–20 show the solution obtained on three successively refined meshes. Both the distributions of skin friction and wall temperature are accurately computed, even with just 25 points in the normal direction. The effect of numerical dissipation intro-

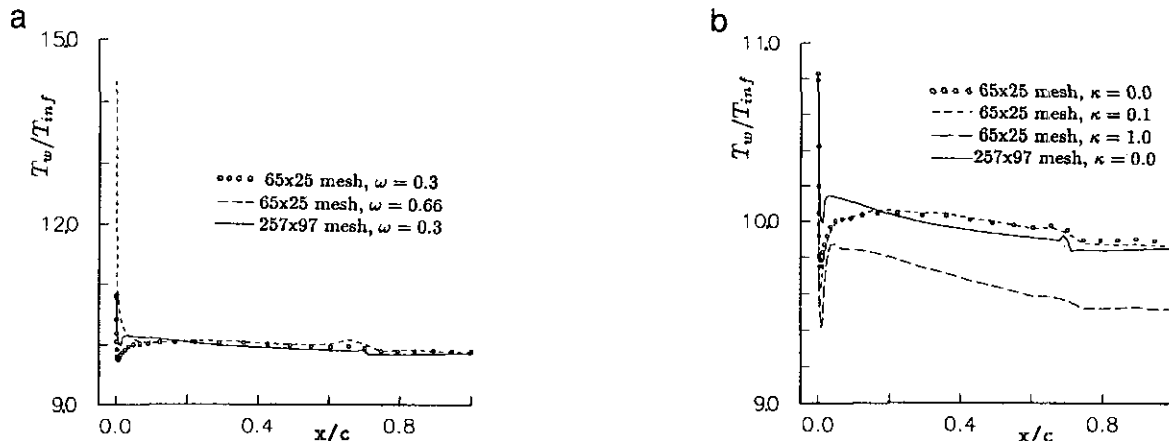


FIG. 21. Influence of the entropy correction coefficients on the adiabatic wall temperature along forebody: (a) Influence of the exponent  $\omega$ ; (b) Influence of the cut-off value,  $\kappa$ , applied to the convective waves.



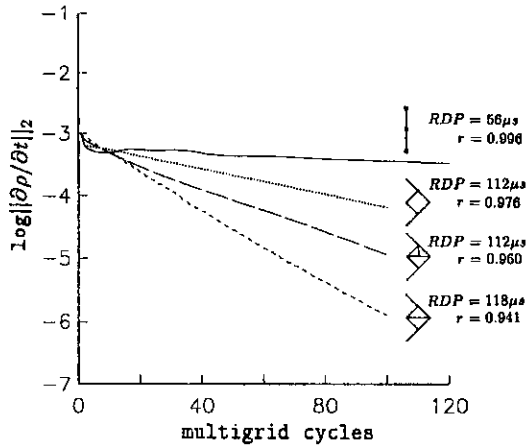


FIG. 22. Influence of multigrid strategy on convergence for forebody, mesh  $256 \times 96$ .

duced by the entropy correction function  $\Psi$ , Eqs. (5.4)–(5.8), is shown in Fig. 21. If the value of  $\omega$  is increased to  $\frac{2}{3}$ , which is a typical value used in central-difference codes [2, 4], the wall temperature is badly reproduced on the coarse mesh. Furthermore, if we introduce numerical dissipation for the convective waves in the direction of the short side of the cells by setting  $\kappa > 0$ , the shear layers are numerically smeared; hence, the wall temperature is adversely affected. We note that a value of  $\kappa = 0.1$ , which again is a representative dissipation level of current central-difference codes, yields reasonable solutions. However, the convergence behavior is not changed much with this relatively low level of numerical dissipation. Hence, all the results presented for the three hypersonic test cases were obtained with a single set of parameters,  $\bar{\delta} = 0.25$ ,  $\omega = 0.3$ , and  $\kappa = 0$ .

Next we investigate the convergence behavior of the multigrid schemes. The fine mesh with  $257 \times 97$  points allows 11 grid levels to be used with semicoarsening. First we note

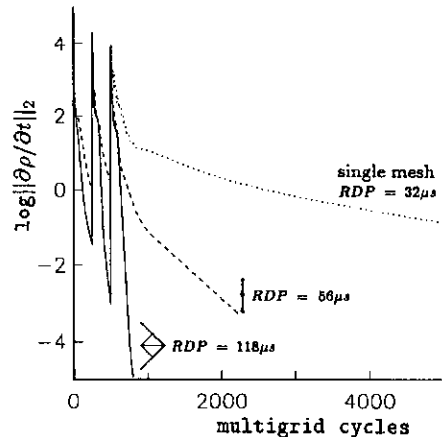


FIG. 23. Convergence histories for single-mesh time stepping and multigrid with sequential semicoarsening.

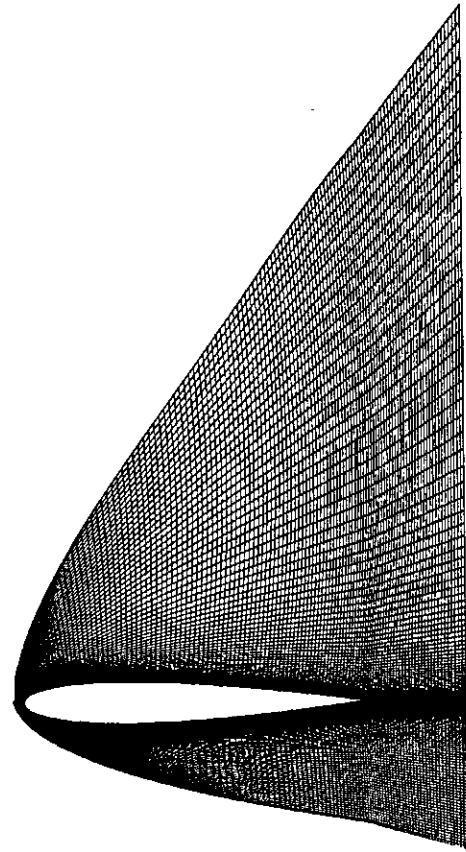


FIG. 24. Coordinate mesh for NACA 0012 with  $256 \times 80$  cells.

that it is not possible to run the full diamond-shape tree of coarse meshes. Obviously, the time-stepping scheme is not well suited to handle the extreme aspect ratios which occur on the  $17 \times 97$  mesh, for example. Using the proper half of the diamond, which includes the meshes with relatively low aspect ratios, the numerical solution converges. Figure 22 displays a comparison of the different multigrid strategies. The computations are started from a pre-converged solution. The computer time to update a grid point by one multigrid cycle, RDP, and the final convergence rate,  $r$ , are also included. Again, the scheme with sequential semicoarsening converges best. The differences between the multigrid schemes for this case, having cells with very high aspect ratios, are larger than for the ramp flow. The final convergence rate of the scheme with sequential semicoarsening is 15 times better than the rate with full coarsening. A comparison of the performance for the complete FMG process is given in Fig. 23. The sequential semicoarsening scheme takes 194 cycles and 570 CPU seconds on a Cray-YMP to reduce the averaged residuals to  $10^{-2}$  on the fine mesh. The scheme with full coarsening takes 1024 cycles and 1430 s, and the single mesh code takes 7762 time steps and 6190 s to achieve the same convergence level. Note that residuals of  $10^{-2}$  correspond to a solution which is converged to engineering

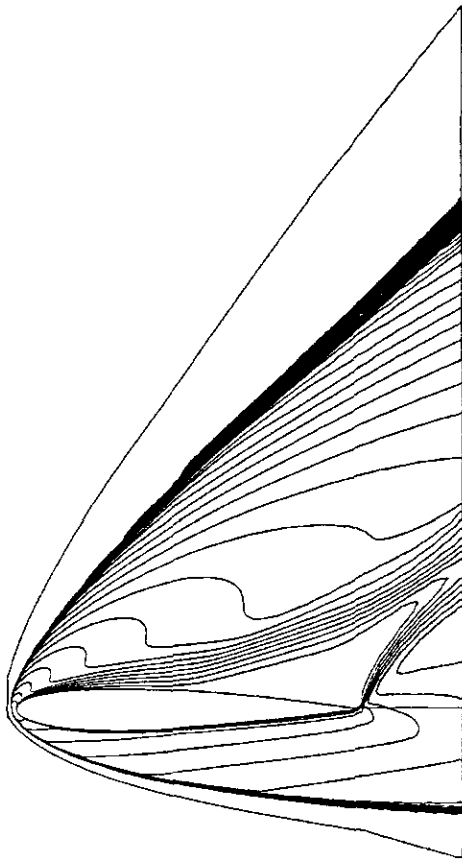


FIG. 25. Mach contours for NACA 0012.

accuracy. If we compared computer times to reach lower levels of residuals, instead, the results would have been even better for the multigrid scheme with semicoarsening.

Laminar flow over an airfoil at  $M = 25$  and  $\alpha = 30^\circ$  is chosen as a test case in order to demonstrate that the multigrid method used here can handle very strong shock waves and highly expanded flow. Figure 24 shows the  $257 \times 81$  mesh.

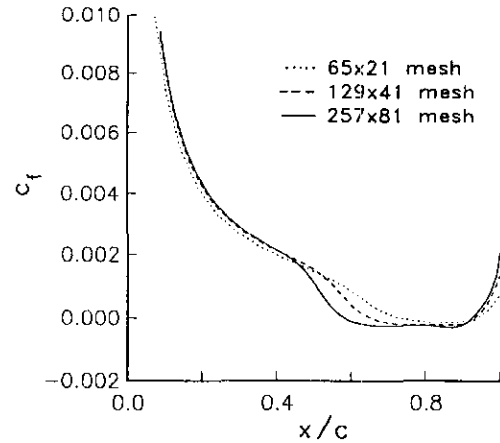


FIG. 27. Distribution of skin friction along airfoil.

The numerical flow solution, which is represented in Figs. 25–28, features a large separated flow region with two distinct vortices. The resulting shear layers are not well aligned with the coordinate mesh; hence, considerable numerical smearing is expected in those regions. The difficulties in resolving this highly separated flow are illustrated by a comparison of the results obtained from meshes with different grid densities. Obviously, the mesh with  $129 \times 41$  points is still too coarse to resolve the separated flow region. The convergence history of the sequential semicoarsening scheme is shown in Fig. 29. The residual drops eight orders of magnitude within 400 multigrid cycles. Note that the largest values of  $\partial p / \partial t$  are located at the shock wave. The solution converges to engineering accuracy within 100 multigrid cycles.

In Figs. 30 and 31 the results for the final case (transonic flow over an RAE 2822 airfoil) are displayed. For this computation the inputs of the numerical scheme (i.e., CFL,  $\delta$ ,  $\omega$ , and  $\kappa$ ) are the same as the usual ones used for the hypersonic flow cases. The results for this turbulent flow include distributions of pressure and skin-friction coefficients, as well as the coefficients of lift ( $C_l$ ), pressure drag ( $C_{dp}$ ), and friction drag ( $C_{df}$ ).

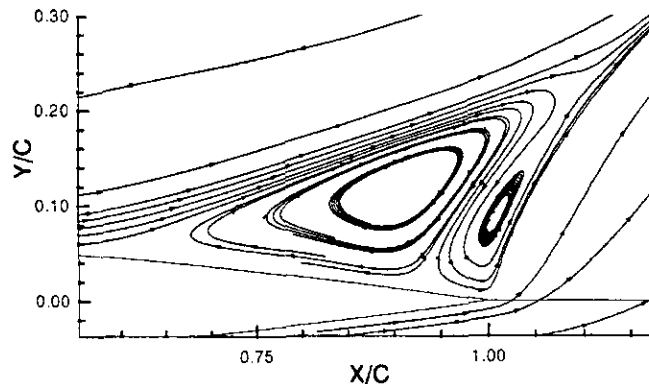


FIG. 26. Streamlines in separated-flow region.

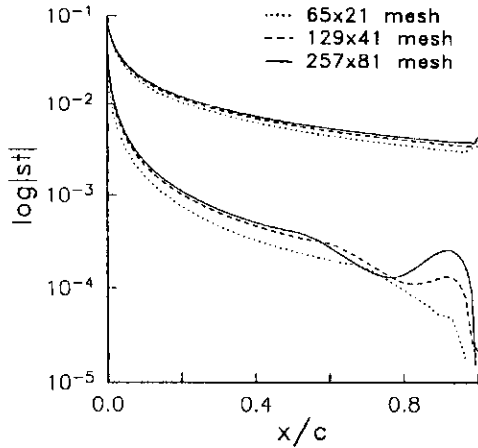


FIG. 28. Distribution of Stanton number along airfoil.

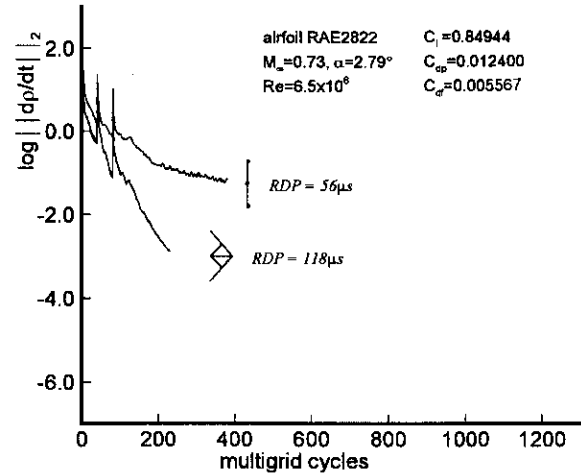


FIG. 31. Convergence behavior for transonic flow over RAE 2822 airfoil ( $M = 0.73$ ,  $\alpha = 2.79^\circ$ ,  $Re = 6.5 \times 10^6$ ).

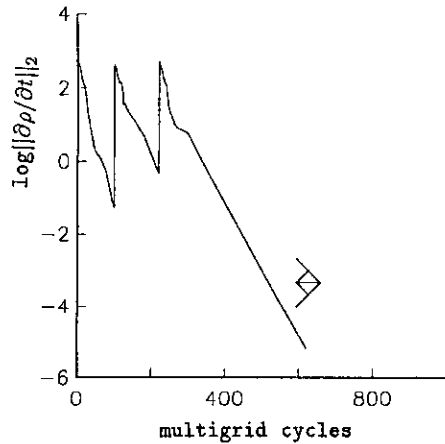


FIG. 29. Convergence history for flow around NACA 0012 airfoil at  $M = 25$ ,  $\alpha = 30^\circ$ .

The predicted distributions exhibit good agreement with the experimental data of [32]. All of the results are comparable to those obtained in [4] with central differencing and twice the present mesh density. Thus, the improved accuracy of the upwind scheme compensates for its higher operation count. The convergence history for this case is also presented in Fig. 31. Again, significant differences in the convergence rates for multigrid with sequential semicoarsening and full coarsening are observed. The convergence rate for the sequential semi-coarsening scheme (0.942 over 150 multigrid cycles) is comparable to those rates reported in [4] for central differencing combined with full coarsening and a W-type cycle.

### 8. CONCLUSIONS

Several multigrid schemes for hypersonic flow computations have been investigated. The basic solution algorithm employs

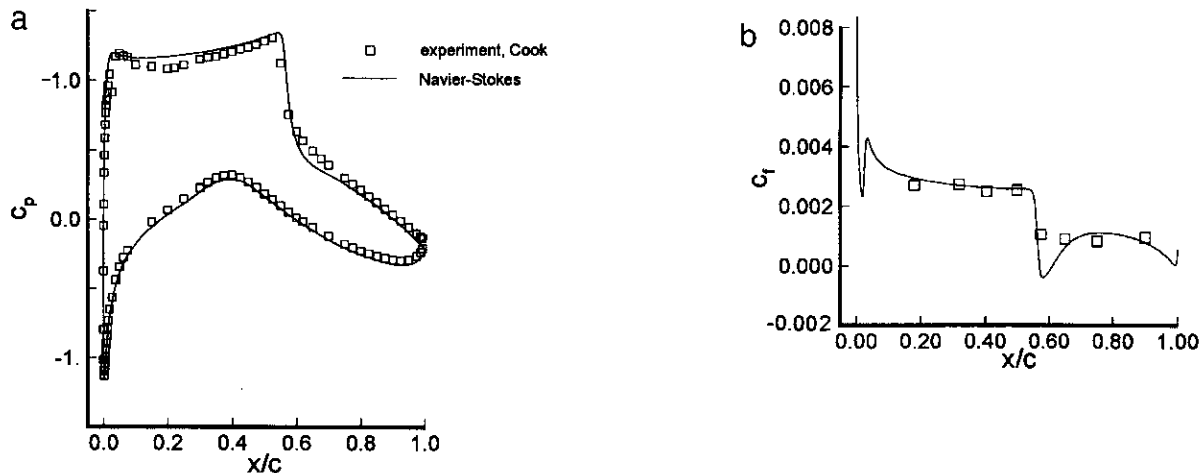


FIG. 30. Solution for transonic flow over RAE 2822 airfoil ( $M = 0.73$ ,  $\alpha = 2.79^\circ$ ,  $Re = 6.5 \times 10^6$ ): (a) pressure coefficient; (b) skin friction.

upwind discretization and explicit multistage time stepping. Various multigrid schemes with semicoarsening are introduced in order to overcome stiffness resulting from the mesh cells with high aspect ratio which are necessary to resolve viscous flows. The basic components of the algorithm are examined with Fourier stability analysis applied to the two-dimensional advection equation. Both the results of the Fourier analysis and the computations of high Reynolds number flows suggest that the semicoarsening approach is effective. For the first time, convergence rates for hypersonic viscous flows are shown which are similar or even better than those previously published for the transonic regime [3, 4]. Further work is required to make the computational scheme less expensive. This is especially true for the coarse meshes used within the semicoarsening approach, which make up the major portion of the overall work count of the scheme. Further improvements of convergence rates seem possible if stiffness arising from the difference of characteristic speeds of acoustic and convective waves can be overcome. For this purpose, new techniques such as preconditioning of the flow equations [30, 31] or characteristic residual smoothing [12] seem to hold promise.

### ACKNOWLEDGMENTS

The present work evolved while the first author stayed at the Institute for Computer Applications in Science and Engineering as a Visiting Scientist. The communications with J. Blazek during the development of the Fourier analysis and many valuable discussions with N. Naik, P. Roe, J. van Rosendale, and E. Turkel are gratefully acknowledged.

### REFERENCES

1. A. Jameson, *Lecture Notes in Mathematics*, Vol. 1228 (Springer-Verlag, Berlin/Heidelberg/New York, 1986), p. 166.
2. L. Martinelli and A. Jameson, AIAA Paper 88-0414, 1988 (unpublished).
3. R. Radespiel, C. Rossow, and R. C. Swanson, *AIAA J.* **28**, 1464 (1990).
4. R. C. Swanson and R. Radespiel, *AIAA J.* **29**, 697 (1991).
5. R. C. Swanson, E. Turkel, and J. A. White, *Commun. Appl. Numer. Methods* **8**, 671 (1992).
6. E. Turkel, R. C. Swanson, V. N. Vatsa, and J. A. White, AIAA Paper 1572-CP, 1991 (unpublished).
7. N. Kroll, D. Gaitonde, and M. Aftosmis, AIAA Paper 91-0636, 1991 (unpublished).
8. R. Radespiel and N. Kroll, Tagungsband 7, DGLR-Fachsymposium "Strömungen mit Ablösung, Aachen, November 7, 1990," DGLR-Bericht 91-5, 1990 (unpublished).
9. R. Radespiel and N. Kroll, DLR-IB 129-90/19, Institute for Design Aerodynamics, Braunschweig, Germany, 1991 (unpublished).
10. N. Decker and E. Turkel, "Multigrid for Hypersonic Inviscid Flows," in *Proceedings, 3rd International Conference on Hyperbolic Problems*, Uppsala, Sweden, 1990 (unpublished).
11. M. P. Leclercq and B. Stoufflet, *J. Comput. Phys.* **104**, 329 (1993).
12. J. Blazek, N. Kroll, R. Radespiel, and C.-C. Rossow, AIAA Paper 1533-CP, 1991 (unpublished).
13. J. L. Thomas, *Commun. Appl. Numer. Methods* **8**, 683 (1992).
14. B. Koren and P. W. Hemker, *Appl. Numer. Math.* **7**, 309 (1991).
15. A. Brandt, *Math. Comput.* **31**, 333 (1977).
16. N. H. Naik and J. Van Rosendale, *SIAM J. Numer. Anal.* **30**, 215 (1993).
17. W. A. Mulder, *J. Comput. Phys.* **83**, 303 (1989).
18. K. Stüben and U. Trottenberg, *Lecture Notes in Mathematics*, Vol. 960 (Springer-Verlag, Berlin/Heidelberg/New York, 1981), p. 1.
19. B. Gustafsson and P. Lötstedt, in *Proceedings, Fourth Copper Mountain Conference on Multigrid Methods*, edited by J. Mandel et al. (SIAM, Philadelphia, 1990), p. 181.
20. B. van Leer, C.-H. Tai, and K. G. Powell, AIAA Paper 1933-CP, 1989 (unpublished).
21. E. Lavante, A. El-Miligui, F. E. Cannizaro, and H. A. Warda, *Notes in Numerical Fluid Mechanics*, Vol. 29, edited by P. Wesseling (Vieweg, Braunschweig, 1990), p. 293.
22. C.-H. Tai, Ph.D. dissertation, Department of Aerospace Engineering, University of Michigan, 1990 (unpublished).
23. B. S. Baldwin and H. Lomax, AIAA Paper 78-257, 1978 (unpublished).
24. H. C. Yee and A. Harten, *AIAA J.* **25**, 266 (1987).
25. P. L. Roe, *J. Comput. Phys.* **43**, 357 (1981).
26. H. C. Yee, *J. Comput. Phys.* **68**, 151 (1987).
27. B. Müller, AIAA Paper 1977-CP, 1989 (unpublished).
28. R. Abgrall, et al., (Eds.), *Hypersonic Flows for Reentry Problems*, Vol. 3 (Springer-Verlag, Berlin/Heidelberg/New York, 1992).
29. W. A. Mulder, *J. Comput. Phys.* **100**, 91 (1992).
30. E. Turkel, *J. Comput. Phys.* **72**, 277 (1987).
31. B. van Leer, W.-T. Lee, and P. Roe, AIAA Paper 1552-CP, 1991 (unpublished).
32. P. H. Cook, M. A. McDonald, and M. C. P. Firmin, AGARD Advisory Report No. 138, 1979 (unpublished).